OPTICA QUANTUM

Scalable low-loss cryogenic packaging of quantum memories in CMOS-foundry processed photonic chips

ROBERT BERNSON,[1,†,7] ALEX WITTE,[2,†,*] GENEVIEVE CLARK,[2,3] KAMIL GRADKOWSKI,[1] JEFFREY YANG,[2] MATT SAHA,[2] MATTHEW ZIMMERMANN,[2] ANDREW LEENHEER,[4] KEVIN C. CHEN,[3] GERALD GILBERT,[5] MATT EICHENFIELD,[4,6] DIRK ENGLUND,[3] AND PETER O'BRIEN[1]

[1]Tyndall National Institute, Lee Maltings Complex, Dyke Parade, T12 R5CP, Cork, Ireland
[2]The MITRE Corporation, 202 Burlington Road, Bedford, Massachusetts 01730, USA
[3]Research Laboratory of Electronics, Massachusetts Institute of Technology, 50 Vassar Street, Cambridge, Massachusetts 02139, USA
[4]Sandia National Laboratories, P.O. Box 5800, Albuquerque, New Mexico 87185, USA
[5]The MITRE Corporation, 200 Forrestal Road, Princeton, New Jersey 08540, USA
[6]College of Optical Science, University of Arizona, Tucson, Arizona 85719, USA
[7]robert.bernson@tyndall.ie
[†]These authors contributed equally.
*awitte@mitre.org

Received 13 March 2025; revised 16 October 2025; accepted 22 October 2025; published 5 December 2025

Optically linked solid-state quantum memories such as color centers in diamond are a promising platform for distributed quantum information processing and networking. Photonic integrated circuits (PICs) have emerged as a crucial enabling technology for these systems, integrating quantum memories with efficient electrical and optical interfaces in a compact and scalable platform. Packaging these hybrid chips into deployable modules while maintaining low optical loss and resiliency to temperature cycling is a central challenge to their practical use. We demonstrate a packaging method for PICs using surface grating couplers and angle-polished fiber arrays that is robust to temperature cycling, offers scalable channel count, applies to a wide variety of PIC platforms and wavelengths, and offers pathways to automated high-throughput packaging. Using this method, we show optically and electrically packaged quantum memory modules integrating all required qubit controls on chip, operating at millikelvin temperatures with <3 dB losses achievable from fiber to quantum memory for the TE_0 mode at a wavelength of 737 nm.

Published by Optica Publishing Group under the terms of the Creative Commons Attribution 4.0 License. Further distribution of this work must maintain attribution to the author(s) and the published article's title, journal citation, and DOI.

https://doi.org/10.1364/OPTICAQ.562093

1. INTRODUCTION

Recent progress in integrated optics has seen the use of optical fibers for scalable, low-loss packaging of PICs [1,2]. Quantum computing systems bring additional requirements for optical packaging, particularly approaches integrating solid-state single-photon sources and memories. Such systems typically require cryogenic temperatures (1), broad wavelength operation (2), and minimal photon loss (3) in order to operate quantum gates with high fidelity. Optical packaging for these systems must also incorporate electrical co-packaging for qubit control and active photon routing (4) while often accommodating high channel count (5) and heterogeneous integration of diverse materials (6) [3] in order to maintain a scalable architecture. However, achieving broadband, efficient coupling between optical fibers and PIC waveguides involves significant engineering and precise alignment to reduce spatial mismatch between the respective optical modes [4]. Differences in thermal expansion among the optical fiber, PIC, and submounts can cause this alignment to shift and fail as devices are cooled to cryogenic temperatures, posing a major obstacle to achieving criteria 1–6.

These challenges have prompted exploration of diverse approaches to achieve effective optical integration of quantum PICs. Several demonstrations have shown cryogenic optical packaging of telecom wavelength PICs using single fibers coupled to grating couplers [5,6], but these approaches cannot accommodate scalable channel count without significant additional time burdens. Multi-channel optically packaged PICs have recently been demonstrated at cryogenic temperatures

using fiber arrays coupled to gratings; however, this relied on strict fabrication tolerances, strain relief structures, and vertical clearance due to the fiber array's angle of incidence [7]. Edge coupling to eight optical channels has been shown in visible wavelength PICs [8], and though this approach is promising, the requirements for mode matching between the PIC and optical fiber reduce the achievable coupling efficiency to heterogeneously integrated quantum memories. Additionally, this method relies on strict fabrication tolerances and strain relief structures to achieve 3 dB coupling efficiency between the fiber array and the PIC. Less established coupling methods including tapered fibers [9–11] and photonic wire bonds [12] have recently led to improved coupling loss and broadband operation at visible wavelengths and cryogenic temperatures. However, these methods require custom equipment or assembly fiber-by-fiber, hindering their practical scalability and prospects of eventual automation as they require many complex, high precision steps to be achieved without a single failure.

Here, we demonstrate a straightforward optical packaging approach using grating couplers and angle-polished fiber arrays compatible with cryogenic operation and wavelengths ranging from visible to telecom. Our process has an alignment tolerance of ±2 µm, is robust to repeated temperature cycling, and is assembled from off-the-shelf components which are widely used in modern industrial telecom applications [1]. This approach places no requirements on the photonic platform itself, allowing us to test over a dozen successful packages from two different foundry processes (see Supplement 1, Section 8). These factors compare favorably to the state of the art, which as mentioned above, are not intrinsically scalable (see Supplement 1, Section 1). We demonstrate the operation of packaged visible and telecom wavelength optical grating loopback structures (waveguides connecting input and output grating couplers) at 6K and room temperature. The grating transmission losses per coupler measured as low as 2.2 dB for visible wavelengths, with potential for further improvement using advanced grating designs. In order to understand and design around the effects of thermal cycling, we also develop a comprehensive model of our fiber-to-grating interface which takes into account thermal, mechanical, and optical considerations. Finally, we apply our approach to foundry-process PICs optimized for low-loss integration of diamond quantum memories. We show successful operation of our packaged PICs down to millikelvin temperatures with diamond to PIC coupling loss <0.5 dB. We demonstrate a first of its kind fully electrically- and optically-packaged active quantum memory module with all required functionality for qubit control including on-chip optical routing and strain tuning present on a single chip.

2. OPTICAL PACKAGING METHOD

Figure 1 shows an overview of our packaging approach for an active, piezoelectric PIC with integrated quantum memories. The PIC [13,14] (Fig. 1(a)) is mounted on a copper submount for thermal contact with the cold finger of a cryostat and wirebonded to a printed circuit board (PCB) for electrical signal delivery to on-chip modulators and control lines. The piezoelectric platform itself (Fig. 1(b)) consists of silicon dioxide-cladded silicon nitride waveguides, with aluminum layers delivering electrical signals to an aluminum nitride piezoelectric layer beneath the SiN waveguides. This platform allows both room temperature

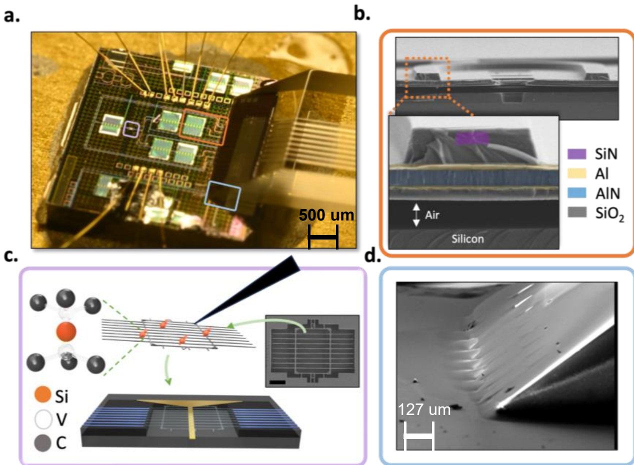

Fig. 1. (a) An optically and electrically packaged quantum PIC mounted on a copper submount and PCB with significant features noted in colored boxes and described in the rest of the figure. Scale bar is 500 µm. (b) Cross-section scanning electron microscope (SEM) images of the piezoelectric modulators used in our photonic chips. (c) Heterogeneous integration of color centers in diamond microchiplets with matching sockets in the PIC. (d) SEM image of an angle-polished fiber array adhered to the PIC after optical packaging. Scale bar is 127 µm.

and cryogenic operation of stable, high extinction modulators for the delivery and collection of photons in quantum PICs. We use a pick-and-stamp method [15] to detach diamond quantum microchiplets (QMCs) hosting group-IV color centers from a parent chip [16] and integrate them into sockets in the piezo-PIC (Fig. 1(c)). These sockets are equipped with exposed SiN waveguides for efficient optical coupling with the QMC waveguides [16,17], electrical lines for microwave spin control [18], and cantilevers for color center strain tuning [19]. Waveguide loopback structures are used to align an angle-polished fiber array with grating couplers on the PIC for optical excitation and fluorescence readout (Fig. 1(d)). These single etch step lensed grating couplers provide a ±2 µm alignment tolerance to HP630 fiber, which is determined by the respective mode field diameters of the coupler and fibers [20]. Finally, we use UV-cured optical epoxy to attach the fiber array to the PIC, yielding a fully packaged, deployable quantum PIC (Fig. 1(d)).

Adhesive selection plays a critical role in the success of our packaged modules at cryogenic temperatures. While commonplace in room-temperature photonic packaging, UV-cured optical adhesives are rarely tested at cryogenic temperatures required for quantum information processing [19]. As a first step in the development of our packaging process, the mechanical performance of five commercially available UV-cured adhesives was benchmarked in ambient conditions and at 7 K. We selected Dymax OP-4-20632 due to its previously demonstrated use in room-temperature optical packaging [21], while the other four candidates were selected based on their advertised performance at 70 K. None of the selected adhesives were advertised to work at temperatures below 70 K, but they were recommended by their individual manufacturers for use in cryogenic applications.

Since delamination and differences in the coefficient of thermal expansion (CTE) within the package can cause changes in optical alignment as a function of temperature, the chosen

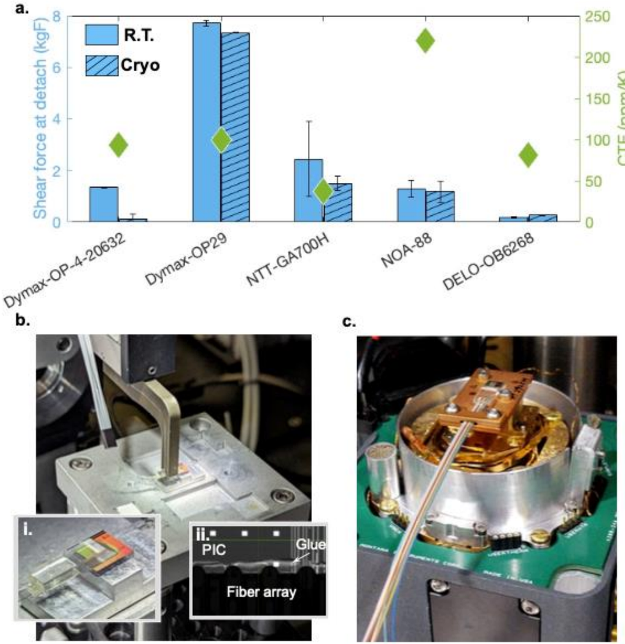

Fig. 2. (a) Average shear bond strength and Coefficient of Thermal Expansion (CTE) measurements for various commercially available optical adhesives tested at room temperature and 7 K. (b) Reference package aligned and cured, (i) fully packaged device released from grippers, (ii) close-up surface image of fiber array attached to PIC via cured Dymax OP-29. (c) A packaged module mounted on the cold finger of a Montana optical cryostat.

figures of merit for each epoxy are shear bond strength and CTE. Details of our testing regimen and tabulated results for shear bond strength are shown in Supplement 1, Section 2. These results, as well as CTE values at room temperature for each of the adhesives, are summarized in Fig. 2(a). The shear force required to detach the Dymax OP-29 sample is greater than 7 kgF with virtually no degradation after temperature cycling, nearly four times higher than the second best performing adhesive (DELO). The refractive index of cured Dymax OP-29 is close to that of SiO_2 (1.50 vs 1.46), and when compared to alternative optically transparent adhesives, it has a relatively short curing time [22]. Due to these properties, as well as its high transparency above 400 nm, Dymax OP-29 was selected for fiber array attachment in our process.

After 6-axis active alignment between the fiber array and the PIC (Fig. 2(b)), a drop of OP-29 adhesive is placed between them, filling the air gap via capillary action [21]. This process confines a majority of the adhesive under the fiber array block, enabling close proximity to sensitive structures on the PIC surface like wirebonds and released MEMs devices (Fig. 2(b(ii))). After final adjustments to the fiber array's position, the output power from the device is continually monitored while the package surface is exposed to low-power UV light until the epoxy is fully cured and ready for cryogenic testing (Fig. 2(c)). Throughout our packaging process, we use automatic stages (Thorlabs NanoTrak) for active alignment optimization as well as an electronically controlled syringe to dispense the epoxy, minimizing the need for human skill and intervention. The initial alignment of the fiber array, placement of the syringe, and UV cure steps are currently manual but can be simply automated via more tightly integrated alignment protocols. This setup provides a clear path to full automation, making it attractive for circumstances where automated and high-throughput operation is desired.

3. RESULTS

Figure 3 shows results from two samples demonstrating our method's compatibility with cryogenic operation, one designed for 1310 nm operation (Figs. 3(a) and 3(c)) and the other for 737 nm (Figs. 3(b) and 3(d)). Both samples consist of PICs with grating-coupled loopback waveguides and an angle-polished fiber array glued to the chip. SMF28 and HP630 fiber were respectively used for the 1310 nm and 737 nm samples. After fiber attachment, the packages are cooled to 6 K while monitoring transmission at the output grating normalized to input power (Figs. 3(a) and 3(b)). We observe slow polarization drift during cooldown which we ascribe to changes in the optical fiber as a function of temperature. At each timestep, we correct for this polarization drift by implementing an automated polarization optimization setup (Supplement 1, Section 3). After polarization correction, both the visible and telecom packages show improved transmission at the measurement wavelength at low temperatures compared to ambient conditions, with no failure or significant drop in transmission as the samples are cooled (Figs. 3(a) and 3(b)). This phenomenon is observed in all measured packages which do not catastrophically fail during the initial cooldown. We record optical spectra for each sample at room temperature and 6 K and observe a reversible blueshift present in both samples upon cooling (Figs. 3(c) and 3(d)), as well as oscillations in the transmission of the visible package as a function of wavelength (Fig. 3(d)). We attribute these oscillations to Fabry–Perot resonances resulting from partial reflections between the bottom of the fiber block and top surface of the PIC, discussed in more detail below and in Supplement 1, Section 4. Both example packages undergo multiple thermal cycles, from room temperature (300 K) down to 6 K and back up to room temperature, in order to record these power and spectral measurements. The packages display no indication of delamination or weakening in the adhesive provided the warming cycle does not shock the package with abrupt heater activation. Supplement 1, Section 8 includes a table of currently packaged devices and their failure modes. We highlight that out of a dozen samples packaged, all survived an initial cooldown, with any subsequent failures due to handling or improper mounting. The sources of these failures are known and have been corrected for, leading to a high package survivability rate. Packaged samples also retain stability once cooled to base temperature for a maximum recorded time of three weeks, with no evidence to show they would not survive indefinitely at cryogenic conditions.

To understand the effects of temperature on our optical packaging, we construct a comprehensive model of the fiber array, adhesive, and visible grating couplers using finite element methods (COMSOL) (Fig. 4, inset). We first build the model in a 3D CAD environment to exactly match our package, combining the grating couplers and fiber array with a layer of adhesive between them such that the pitch of the fiber array matches our physical device at room temperature. We then use a thermal simulation to determine the geometry of our package at room temperature (300 K) and cryogenic temperature (6 K) to track any changes as the assembly is cooled. Finally, we use an optical simulation

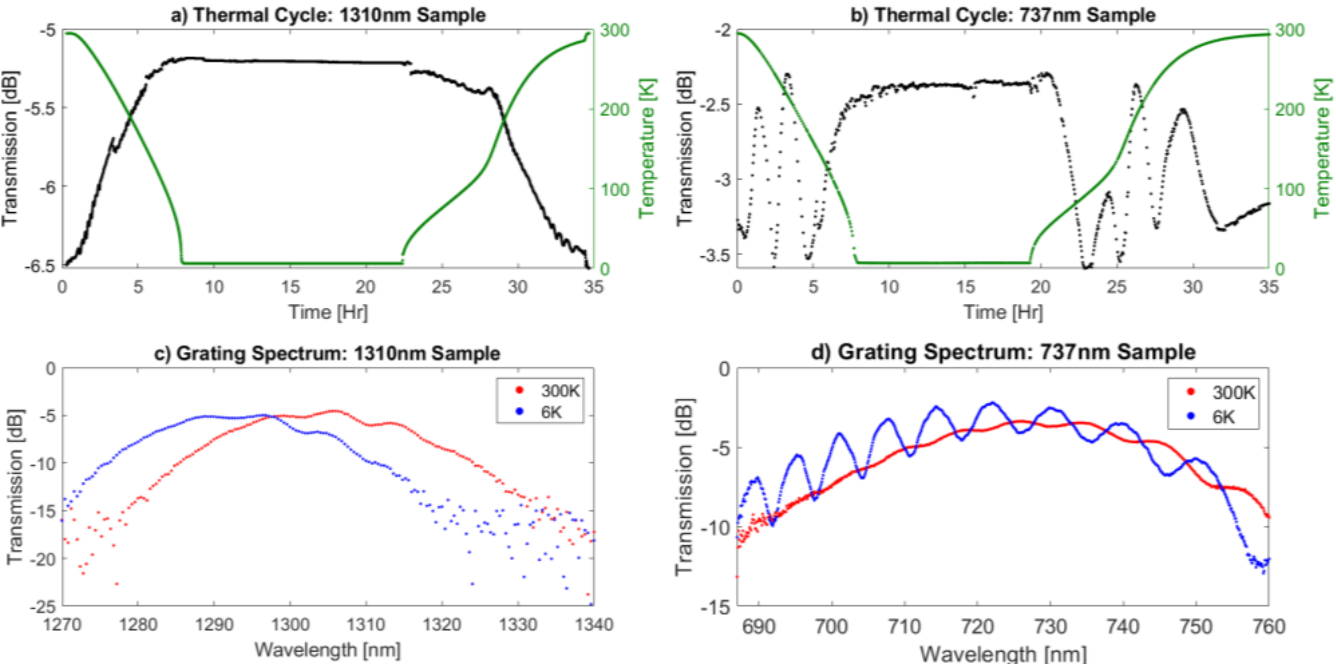

Fig. 3. Packaging performance under cryogenic conditions. (a) Thermal cycling of optically packaged 1310 nm grating couplers, measured at 1300 nm. After an angle-polished fiber is glued to a grating loopback, the PIC is placed in a cryostat and cooled to 6 K. Grating efficiency is measured during a full thermal cycle, holding 6 K for a total of 15 hours. (b) Thermal cycling of optically packaged 737 nm grating couplers, measured at 730 nm. During cycling, fiber shrinking causes polarization rotation, requiring constant re-optimization. (c) Spectral response of the 1310 nm gratings at room temperature as well as 6 K. A 9 nm blueshift is observed. (d) Spectral response of the 737 nm gratings at room temperature as well as 6 K. A 1 nm blueshift is observed.

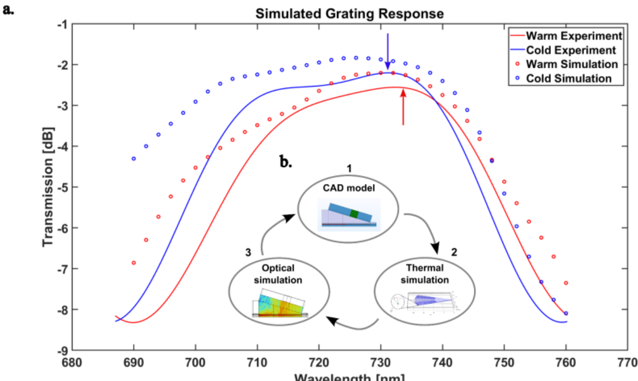

Fig. 4. (a) Simulated grating coupler spectral response at room temperature and 6 K. Oscillations due to Fabry–Perot effects have been removed. The experimentally measured 1 nm shift in peak transmission wavelength at 6 K corresponds to a 2° decrease in fiber pitch angle, as determined by optical simulations. (b) Illustration of the simulation cycle used in this work. First, a model of the package is constructed. Thermal effects are then simulated and followed by optical spectrum simulations.

for the resulting geometry to determine the transmission spectrum for the package at room temperature (300 K) and cryogenic temperature (6 K) (Fig. 4(b)).

Figure 4(a) shows an overlay of the simulated (open circles) and measured (filled circles) responses at 6 K and room temperature (we fit and remove the effects of Fabry–Perot resonances), indicating close agreement between the simulated and measured frequency shift in transmission. We measure a difference of 0.3 dB between the simulated maximum grating transmission and the experimentally measured fully packaged sample, indicating close alignment between simulation and our fabricated results. We observe through the thermal simulation that, due to the large CTE of the adhesive compared to the fiber and PIC, thicker sections of adhesive contract more than thinner ones during cooling. This results in a change in pitch of the fiber array if there is any initial variation in the thickness of the adhesive layer. This change in pitch results in a temperature-dependent change in incident angle of light onto the grating coupler, causing a corresponding shift in the transmission spectrum with temperature. We simulated an initial offset of 3° in the pitch angle of the fiber array corresponding to a +2° shift in the incident angle after cooldown. This shift in incident angle corresponds to a blueshift in the simulated optical spectra, consistent with our measurements. Since the increase in coupling efficiency and shift in optimal wavelength seems to arise due to the slight change in incidence angle with temperature, we can improve our method to include either a pre-compensation shift in the incident angle prior to curing the adhesive, or variations in the grating structure to function optimally under the low temperature angle of incidence. Using this multi-physics simulation of the whole packaging interface, we are currently working on providing optimal grating designs, fiber types, and adhesive orientations for a broad range of wavelengths. With this tool, we can apply this process optimally to any number of PIC platforms at any number of wavelengths.

We also observe a change in period of the Fabry–Perot oscillations in the visible sample as it cools to 6 K (Fig. 3(d)), which we attribute to the shortening distance between the fiber array and the PIC surfaces as the adhesive shrinks. By analyzing these

oscillations as a Fabry–Perot cavity (Supplement 1, Section 4), we determine that the cavity length at room temperature is 8.967 ∓ 0.004 μm and 8.579∓0.088 μm at 6 K. These cavity lengths are consistent with our thermal simulations which estimate a 410 nm shrinkage of the adhesive layer between 300 K and 6 K.

4. APPLICATION TO INTEGRATED QUANTUM MEMORIES

We next apply our optical packaging approach to quantum memory modules consisting of diamond quantum microchiplets (QMCs) heterogeneously integrated into CMOS-process photonic chips. We use grating-coupled optical loopback structures (Fig. 5(a)) to establish the process and quantify optical losses arising from heterogeneous integration. QMCs hosting silicon vacancy color centers are integrated into sockets in the center of each loopback, where a window etch removes the oxide overcladding, allowing direct contact between the QMC and SiN waveguides (Fig. 5(a(i) and (ii))). We determine a loss in transmission as low as −0.03 dB at each window transition and −0.43 dB at each diamond-SiN transition for well aligned QMCs, based on transmission of a 737 nm laser (Supplement 1, Fig. 8). With modest grating coupler performance (5 dB loss per coupler at 737 nm) this yields a fiber-PIC-QMC interface with less than 6 dB total loss from fiber to memory, with the potential for losses under 3 dB with high performing grating couplers detailed above (see Fig. 3). While 6 dB of loss is not sufficient for practical single-photon routing in a quantum system, it is acceptable for excitation, where losses in pump light do not impact fidelity. Grating coupler designs with losses of −0.34 dB per coupler [22] have been demonstrated and are fully compatible with this packaging technique, as it relies solely on the presence of surface grating couplers and not on platform specific materials. Measurements taken before and after packaging are consistent with independent non-packaged grating measurements used to quantify grating efficiency. These measurements, along with close agreement between measured and simulated couplers, suggest that loss comes nearly exclusively from the gratings themselves. Any improvements to the gratings will be directly observed in the optical efficiency of this packaging technique, regardless of how the grating structure is designed. Further improvements to the grating coupler design on our platform are currently being investigated using apodized designs and partial-height waveguide etch features.

After determining transmission efficiency, we measure fluorescence from silicon vacancy color centers (SiVs) in our optically packaged module under off-resonant excitation at 532 nm delivered in free-space, with the sample held at 5 K in a Montana cryostat. We observe a clear signal from the SiV ZPL at 737 nm [23] collected through the on-chip waveguides and attached optical fiber (Fig. 5(b)). We next mount the same sample in a 400 mK sorption fridge with no free-space optical access and collect the phonon sideband (PSB) emission from SiVs excited resonantly through the on-chip waveguides. A fiber beam splitter combines a 640 nm laser with the resonant signal to provide alternating resonant and repump pulses. We observe multiple SiVs with high optical quality (Fig. 5(c)) within a single waveguide in the QMC.

Finally, we apply our optical packaging technique to an active, memory-integrated PIC with electrical packaging for color center control and on-chip optical modulation, demonstrating

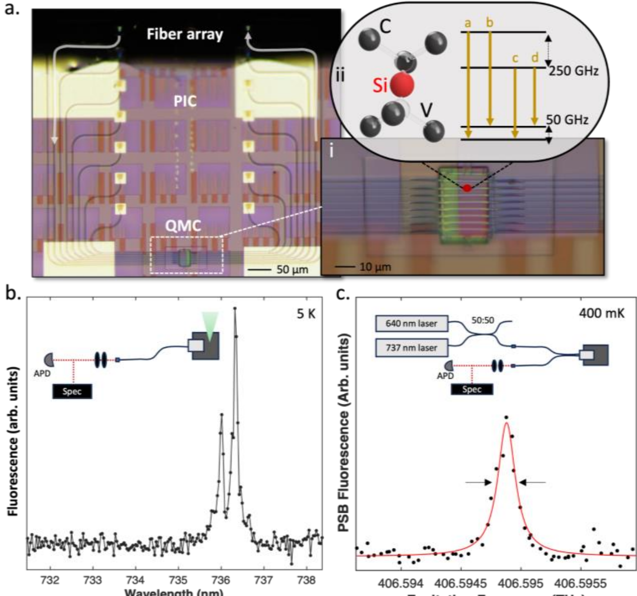

Fig. 5. Optically packaged diamond loopback chip measured at 400 mK. (a) Optical microscope image of a PIC with loopback structures connected through a heterogeneously integrated QMC. An angle-polished fiber array glued to the PIC couples light into the PIC and collects fluorescence from silicon vacancy color centers in the QMC. (i) Zoom-in of the QMC-PIC coupling region. Adiabatic tapering on the SiN and diamond provides high efficiency coupling between the SiN waveguides and aligned diamond nanobeams. (ii) SiV structure, showing four spin-orbit split optical transitions (transitions a,b,c,d depicted on the right). (b) Photoluminescence spectrum measured from SiVs in the integrated QMC showing the SiV ZPL at 737 nm. (c) Phonon sideband fluorescence from resonantly excited SiVs in the PIC, measured at 400 mK with on-chip excitation and collection (measured optical linewidth is 200 MHz).

its compatibility with all-on-chip PIC technologies. Figure 6(a) shows an image of the packaged PIC on a copper mount, wirebonded to a PCB for electrical signal routing. Within the PIC (Fig. 6(b)), double piezoelectric cantilever modulators [14] allow high-contrast modulation of resonant laser input at 737 nm. A parallel input channel combines 532 nm laser input with the 737 nm path at a dichroic beamsplitter, directing both wavelengths into the QMC. SiV fluorescence is collected from the QMC into the on-chip SiN waveguides and directed into a single cantilever modulator and onto two single-photon detectors. Within the socket for the QMC, cantilevers mechanically contacting the diamond chiplet apply controllable strain to SiVs in the QMC for frequency tuning [19,24,25]. In total, there are eight optical gratings for this PIC: two 532 nm inputs, two 737 nm inputs, two optical outputs to collect PLE, and two optical loopback ports.

Figure 6(c) shows photoluminescence excitation (PLE) spectra from three SiVs in two channels of the QMC (i,ii) with frequency control to overcome inhomogeneity in their transition energies (Fig. 6(c(ii))). On-chip modulators and dichroic beamsplitters in the excitation path deliver resonant and off-resonant laser light to the SiVs without requiring a free-space beam or bulky off-chip modulators (Fig. 6(d(i))). This allows both off-resonant excitation at 532 nm (Supp. Fig. 10) and

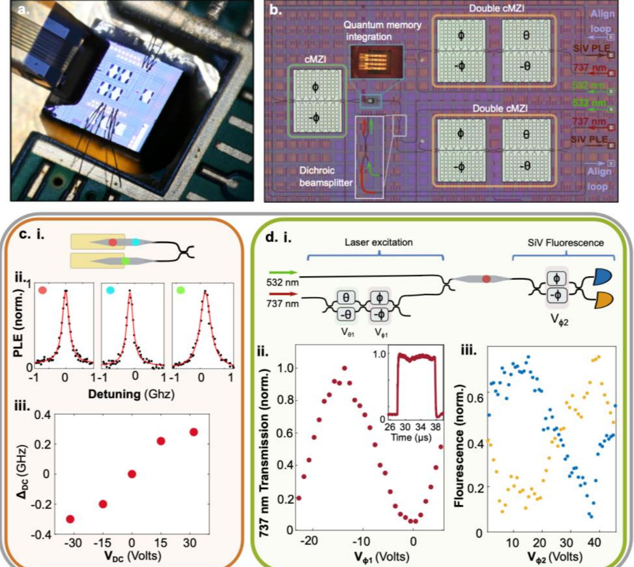

Fig. 6. Electrically and optically packaged chip with integrated diamond. (a) Optical image of the electrically and optically packaged PIC with integrated quantum memories. (b) Zoom-in showing the QMC-integrated PIC, including cantilevers for strain control of quantum memories and optical modulators for control of excitation and collection optical paths. (c) (i) Sketch showing location of three SiVs in two channels of the integrated QMC. (ii) PSB fluorescence from SiVs in channels 3 and 4 of the QMC collected through the attached fiber array. (iii) The integrated cantilevers allow frequency shifting of the ZPL transition to overcome inhomogeneities between color center transition energies. (d) (i) Sketch of device layout for a single channel in the QMC. Two input channels allow both off-resonant excitation or optical repump using a 532 nm laser, and resonant excitation using 737 nm light. (ii) A double cantilever MZI (cMZI) in the 737 nm path modulates the excitation power or generates optical pulses for resonant excitation. The two excitation channels are combined at a dichroic beamsplitter and directed into the QMC. (iii) A cMZI at the output modulates fluorescence from SiVs between two detection channels for autocorrelation measurements and single-photon routing.

high-contrast modulation and pulsing of resonant 737 nm excitation (Fig. 6(d(ii))). Applying a DC voltage to the cMZI in the collection path allows high-contrast optical routing of SiV fluorescence between the two output ports (Fig. 6(d(iii))) and can function as an on-chip beamsplitter for coincidence counting or interference of photons from adjacent channels in the QMC. Our fiber packaging method allows integration of all optical modulation and qubit control components on chip without the need for active fiber alignment or free-space optical access, while multiplexed excitation and readout channels allow scaling to large numbers of spin qubits in future work within a deployable, packaged module.

5. CONCLUSION

In conclusion, we demonstrate a robust and straightforward optical packaging approach that is compatible with cryogenic operation, heterogeneous integration, and electrical co-packaging. Grating couplers at visible and telecom wavelength allow for scalable optical packaging to arrays of single-mode fibers, while high shear-strength epoxy (Dymax OP-29) provides a fiber array-PIC bond that is resilient to repeated temperature cycling. Our approach does not require a thick oxide cladding for optimal mode matching which allows for the low-loss heterogeneous integration of quantum emitters and memories as well as other photonic materials [26–28]. This approach is also compatible with any foundry process that allows the construction of top-surface grating couplers and offers a pathway to automated, high-throughput optical packaging of PICs. We demonstrate the utility of our approach by packaging CMOS-foundry process PICs with heterogeneously integrated quantum memories hosted in diamond QMCs. Loopback structures reveal a fiber-PIC-memory interface with achievable losses below 3 dB while remaining compatible with electrical co-packaging and active photonic structures for routing and color center control. We demonstrate a fully packaged module with 6 dB losses measured from fiber to quantum memory, on-chip resonant and off-resonant excitation, active routing of color center fluorescence, and strain tuning. With improved grating design, we expect that fiber-PIC-memory losses significantly lower than 3 dB are achievable.

Funding. Science Foundation Ireland (SFI-12/RC/2276_P2); Basic Energy Sciences (DE-SC0012704); National Science Foundation; Center for Integrated Nanotechnologies; Office of Science; Sandia National Laboratories (DE-NA0003525).

Acknowledgment. This research was funded by the Taighde Éireann—Research Ireland (formerly Science Foundation Ireland, SFI-12/RC/2276_P2). Major funding for this work is provided by MITRE for the Quantum Moonshot Program. D.E. acknowledges partial support from Brookhaven National Laboratory, which is supported by the U.S. Department of Energy, Office of Basic Energy Sciences, under Contract No. DE-SC0012704 and the NSF RAISE TAQS program. Support is also acknowledged from the U.S. Department of Energy, Office of Science, National Quantum Information Science Research Centers, Quantum Systems Accelerator. M.E. performed this work, in part, with funding from the Center for Integrated Nanotechnologies, an Office of Science User Facility operated for the U.S. Department of Energy Office of Science. Sandia National Laboratories is a multimission laboratory managed and operated by National Technology Engineering Solutions of Sandia, LLC, a wholly owned subsidiary of Honeywell International Inc., for the U.S. Department of Energy's National Nuclear Security Administration under contract DE-NA0003525. This paper describes objective technical results and analysis. Any subjective views or opinions that might be expressed in the paper do not necessarily represent the views of the U.S. Department of Energy or the United States Government.

Disclosures. D.E. is a Scientific Advisor to and holds shares in QuEra Computing. The other authors declare no competing interests.

Data availability. Data underlying the results presented in this paper are not publicly available at this time but may be obtained from the authors upon reasonable request.

Supplemental document. See Supplement 1 for supporting content.

REFERENCES

1. L. Carroll, J.-S. Lee, C. Scarcella, *et al.*, "Photonic packaging: transforming silicon photonic integrated circuits into photonic devices," NATO Adv. Sci. Inst. Ser. E Appl. Sci. **6**, 426 (2016).
2. L. Ranno, P. Gupta, K. Gradkowski, *et al.*, "Integrated photonics packaging: challenges and opportunities," ACS Photonics **9**, 3467–3485 (2022).
3. G. Moody, V. J. Sorger, D. J. Blumenthal, *et al.*, "2022 Roadmap on integrated quantum photonics," J. Phys. Photonics **4**, 012501 (2022).

4. R. Marchetti, C. Lacava, L. Carroll, *et al.*, "Coupling strategies for silicon photonics integrated chips," Photonics Res. **7**, 201–239 (2019).
5. T. P. McKenna, R. N. Patel, J. D. Witmer, *et al.*, "Cryogenic packaging of an optomechanical crystal," Opt. Express **27**, 28782–28791 (2019).
6. W. W. Wasserman, R. A. Harrison, G. I. Harris, *et al.*, "Cryogenic and hermetically sealed packaging of photonic chips for optomechanics," Opt. Express **30**, 30822–30831 (2022).
7. D. Witt, L. Chrostowski, and J. Young, "Packaged cryogenic photon pair source using an effective packaging methodology for cryogenic integrated optics," Appl. Phys. Lett. **127**, 021105 (2025).
8. D. J. Starling, K. Shtyrkova, I. Christen, *et al.*, "Fully packaged multichannel cryogenic quantum memory module," Phys. Rev. Appl. **19**, 064028 (2023).
9. B. Zeng, C. De-Eknamkul, D. Assumpcao, *et al.*, "Cryogenic packaging of nanophotonic devices with a low coupling loss <1 dB," Appl. Phys. Lett. **123**, 161106 (2023).
10. M. Zhao and K. Fang, "Low-loss adiabatic fiber-optic coupler for cryogenic photonics," Appl. Opt. **62**, 9036–9040 (2023).
11. R. A. Parker, J. Arjona Martínez, K. C. Chen, *et al.*, "A diamond nanophotonic interface with an optically accessible deterministic electronuclear spin register," Nat. Photonics **18**, 156–161 (2024).
12. B. Lin, D. Witt, J. F. Young, *et al.*, "Cryogenic optical packaging using photonic wire bonds," APL Photonics **8**, 126109 (2023).
13. P. R. Stanfield, A. J. Leenheer, C. P. Michael, *et al.*, "CMOS-compatible, piezo-optomechanically tunable photonics for visible wavelengths and cryogenic temperatures," Opt. Express **27**, 28588–28605 (2019).
14. M. Dong, D. Heim, A. Witte, *et al.*, "Piezo-optomechanical cantilever modulators for VLSI visible photonics," APL Photonics **7**, 051304 (2022).
15. K. C. Chen, I. Christen, H. Raniwala, *et al.*, "A scalable cavity-based spin–photon interface in a photonic integrated circuit," Optica Quantum **2**, 124–132 (2024).
16. N. H. Wan, T.-J. Lu, K. C. Chen, *et al.*, "Large-scale integration of artificial atoms in hybrid photonic circuits," Nature **583**, 226–231 (2020).
17. S. L. Mouradian, T. Schröder, C. B. Poitras, *et al.*, "Scalable integration of long-lived quantum memories into a photonic circuit," Phys. Rev. X **5**, 031009 (2015).
18. D. A. Golter, G. Clark, T. El Dandachi, *et al.*, "Selective and scalable control of spin quantum memories in a photonic circuit," Nano Lett. **23**, 7852–7858 (2023).
19. G. Clark, H. Raniwala, M. Koppa, *et al.*, "Nanoelectromechanical control of spin–photon interfaces in a hybrid quantum system on chip," Nano Lett. **24**, 1316–1323 (2024).
20. K. Gradkowski, "Tolerances of the alignment of fibers to photonic integrated circuits," Appl. Opt. **63**, 8407–8412 (2024).
21. B. Snyder and P. O'Brien, "Packaging process for grating-coupled silicon photonic waveguides using angle-polished fibers," IEEE Trans. Compon. Packaging Manuf. Technol. **3**, 954–959 (2013).
22. H. Wang, Y. Zuo, X. Yin, *et al.*, "Ultralow-loss optical interconnect enabled by topological unidirectional guided resonance," Sci. Adv. **10**, eadn4372 (2024).
23. D. D. Sukachev, A. Sipahigil, C. T. Nguyen, *et al.*, "Silicon-vacancy spin qubit in diamond: a quantum memory exceeding 10 ms with single-shot state readout," Phys. Rev. Lett. **119**, 1–6 (2017).
24. S. Meesala, Y.-I. Sohn, B. Pingault, *et al.*, "Strain engineering of the silicon-vacancy center in diamond," Phys. Rev. B **97**, 205444 (2018).
25. S. Maity, L. Shao, Y. I. Sohn, *et al.*, "Spectral alignment of single-photon emitters in diamond using strain gradient," Phys. Rev. Appl. **10**, 1–7 (2018).
26. S. Ghosh, S. Yegnanarayanan, D. Kharas, *et al.*, "Wafer-scale heterogeneous integration of thin film lithium niobate on silicon-nitride photonic integrated circuits with low loss bonding interfaces," Opt. Express **31**, 12005–12015 (2023).
27. L. Chang, M. H. P. Pfeiffer, N. Volet, *et al.*, "Heterogeneous integration of lithium niobate and silicon nitride waveguides for wafer-scale photonic integrated circuits on silicon," Opt. Lett. **42**, 803–806 (2017).
28. M. Churaev, R. N. Wang, A. Riedhauser, *et al.*, "A heterogeneously integrated lithium niobate-on-silicon nitride photonic platform," Nat. Commun. **14**, 3499 (2023).

37.5.240.54 2025-12-20 11:25:56